


Numerical Study of Train-induced Pressure on Platform Screen Doors of a Subway Station

Lingwei Zeng^{1,3} · Hanfeng Wang^{1,2}  · Si Peng^{1,4} ·
Feng Cui¹ · Wei Guo^{1,2} · Hui Tang³

Received: 12 January 2023 / Revised: 16 March 2023 / Accepted: 21 March 2023 / Published online: 3 May 2023
© The Author(s) 2023

Abstract We numerically investigate the train-induced transient pressure on the platform screen doors (PSDs) of an island-type platform in a subway station according to real scenarios and full-scale simulation to enhance understanding of the design and safe operation of subway trains. Two typical cases, namely, the non-stop and chasing cases, were examined, with the train's speed variation well simulated throughout both cases. In the non-stop case, a train passes through the station without stopping; in the chasing case, a train stops at the station while another subsequent train approaches through the tunnel, which inevitably happens during rush hours. It is observed that the train generates a compression wave when it passes the tunnel's ventilation shaft, similar to what occurs when entering a tunnel. In the non-stop case, the PSDs experience two positive and one negative pressure extremes in the whole process. The first positive peak results from an oncoming compression wave through the tunnel, while the second positive and negative peaks arise due to the passing of the train head and tail, respectively. In the chasing case, the stopped train at the platform leads to a blockage effect that significantly increases

the pressure on the PSDs via the oncoming compression wave. This lateral pressure may result in the failure of proper operation of the PSDs, particularly during rush hours, with pressure lasting for roughly 5.7 seconds. It is also found that, compared to the fully sealed PSD, both the half-height and partial porous PSDs can significantly reduce the pressure load caused by the passing of the train head, with its maximum pressure load reduced by 38.7% and 38.2%, respectively. Therefore, if the pressure load on a fully sealed PSD is too high for structural design, one may consider the use of half-height and partial porous PSDs as an alternative. Our study offers crucial insights into the train-induced transient pressure on PSDs in a subway station island-type platform. It provides guidance on optimizing the pressure/operation problem on PSDs and offers valuable information for the safe design and operation of subway trains.

Keywords Subway station · Platform screen door (PSD) · Pressure wave · Pressure load · Moving mesh technique

1 Introduction

The platform screen door (PSD) is an indispensable component of the metro system that is widely used to protect passengers and guarantee comfortable circumstances inside the station [1–3]. Since the higher running speed and departure frequency of subway trains have become a more realistic demand during rush hours, the induced extreme pressure is significantly increased, which affects the PSD's structural safety and normal operation.

The structure design for PSDs usually considers the lateral load caused by the crowd, wind pressure, seismic effects, etc. [4], which considers the static or equivalent static load effects on the PSDs. However, a new issue arises

✉ Hanfeng Wang
wanghf@csu.edu.cn

¹ School of Civil Engineering, Central South University, Changsha 410075, China

² National Engineering Laboratory for High-speed Railway Construction, Changsha 410075, China

³ Research Center for Fluid-Structure Interactions, Department of Mechanical Engineering, The Hong Kong Polytechnic University, Kowloon 999077, Hong Kong, China

⁴ Center for Turbulence and Control, Harbin Institute of Technique (Shenzhen), Shenzhen 518055, China

Communicated by Liang Gao.

for the proper operation of PSDs, particularly during the rush hours of the metro system. Specifically, the PSDs may accidentally not open or close appropriately for passengers to board and alight when a train stops in the station [5]. A possible reason for this failure, as reported by Zeng et al. [6] based on their moving model test result, is a lateral load acting on the PSDs, which increases the friction resistance during its opening or closing. Obviously, this lateral force cannot be ascribed to the stopped train at the platform. Instead, it would be associated with the aerodynamic effects induced by the train coming through the tunnel. However, the characteristics and mechanism of this lateral load are not yet fully understood.

Extensive investigations have been conducted on the aerodynamic phenomena caused by a train passing through a tunnel or station [6–11]. A compression wave is generated once the train head enters a tunnel [12, 13], which propagates in the tunnel at the speed of sound. In addition, an expansion wave is produced when the train tail reaches the entrance of the tunnel. The train-induced compression wave is converted to an expansion wave when it arrives at the tunnel exit, and then reflects back into the tunnel [14, 15]. Matsuo and Aoki [16] proposed a model to predict the decaying of compression waves through a tunnel. Ricco et al. [17] experimentally and numerically studied the pressure waves caused by a high-speed train. The influence of the blockage ratio β , namely the ratio between the cross-sectional areas of the train and tunnel, and the train length was discussed. They found that the pressure waves are planar waves with their peak depending almost linearly on β . However, both the length and sectional shape of the train have negligible effects on the strength of the pressure waves.

Moreover, Mei [18] numerically studied the pressure waves generated by a train passing through a tunnel and two trains passing by each other inside a tunnel. For the first case, he suggested the positive and negative extreme pressure in the tunnel appear at the arrival of the train head and tail, respectively. These pressure extrema in the second case increase by approximately 50% and 30%, respectively. More recently, Meng et al. [19] suggested that the peak pressure inside a tunnel caused by a passing train can be reduced by 36% if a ventilation shaft is opened at the center of the tunnel. A similar observation has also been reported by Zeng et al. [6].

With the increase in subway train speed, a growing number of investigations have concentrated on the pressure load on PSDs, especially for the case of a non-stop train passing through an underground station. Chun et al. [7] used the PHOENICS (Parabolic, Hyperbolic or Elliptic Numerical Integrated Code Series) commercial code to investigate the transient pressure on the PSDs induced by a non-stop train.

They found that the pressure on the PSDs is linearly dependent on the square of the train speed, and the maximal pressure appears at the entrance of the station. This observation was further confirmed by Luo [20]. Kim [21] studied the transient pressure on the PSDs through field experiments. He compared three typical cases, i.e., a non-stop train passing through a station, two non-stop trains meeting in a station, and a non-stop train passing through a station while another train is stopped at the platform. He found that the pressure on the PSDs is the highest in the second case and the lowest in the first one. Interestingly, Kim [21] found that the pressure on the PSDs starts to increase when the train is still about 500 m from the platform. Based on a moving model test, Zhou et al. [22] also studied the aerodynamic characteristics of the PSDs for a train passing through a station and two trains passing each other inside a station. They suggested that the maximal pressure on the PSDs occurs near the entrance of the station, which decreases slightly along the platform. Moreover, the maximal pressure on the PSDs for the case with two trains meeting at the center of the station is about 1.22 times higher than that in the first case.

More recently, based on the sliding mesh technique, Yuan et al. [13] numerically studied the transient pressure on the PSDs caused by a non-stop train passing an island-type platform. They found that the maximal pressure on the PSDs quickly decreases with the increasing gap between the train and PSDs. For example, when the gap increases from 130 to 425 mm, the lateral force and overturning moment on the PSDs decrease by 52.72% and 54.71%, respectively. Liang et al. [23] studied the effects of the height of PSDs on the aerodynamic characteristics of both the train and PSDs. With the height of PSDs increasing from 2.5 to 3.75 m and 5 m, the maximum pressure increases by approximately 16.6% and 59.1%, respectively. Based on experimental and numerical results, Zhou et al. [3] suggested that the ventilation shafts near the station entrance and exit can markedly reduce the pressure load on the PSDs inside the station.

Using a moving model test facility, Zeng et al. [6] studied the pressure transient on the PSDs for the chasing case, i.e., a train stopping at the station while a subsequent train is approaching through the tunnel. They suggested that the blockage brought by the stopped train results in an increase in the pressure load on the PSDs through the interaction of the compression wave induced by the coming train. However, because of the length limitation of the moving model facility, there were still some noticeable differences between their test and a real subway operation scenario, including the length of the tunnel, the spacing between the coming train and stopped train, and the variation in the train velocity throughout the process. In addition, rare studies have focused on the effect of different forms of PSDs on the

resulting pressure. These opening questions motivated us to carry out the following research work.

This paper reports a systematic numerical investigation of the aerodynamic characteristics of PSDs of an island-type platform. Two typical cases were studied, i.e., the non-stop case and the chasing case. In non-stop cases, a train passes the station without stopping. In the chasing cases, a train stops at the platform, while a subsequent train approaches through the tunnel. The studied model of the train, station, and tunnel are all based on their corresponding prototypes widely used in real metro systems. In addition, the variation in train speed during the whole process is identical to the real scenario. Moreover, for the non-stop cases, three types of PSDs, i.e., fully sealed, half-height, and partial porous, and the status of the ventilation shafts were also simulated to investigate their influence on the pressure on PSDs. This study provides in-depth insight into the train-induced pressure on the PSDs under two typical operating scenarios and

three different forms of PSDs, which may offer some guidance on the optimization of the relevant pressure problem on the PSD.

2 Numerical Modeling

2.1 Computational Model

The model of the station with an island-type platform is given in Fig. 1. The total length, width, and height are 233.2 m, 28.45 m, and 6.5 m, respectively. The PSDs along the platform are highlighted in blue. Their total length and height are 166.15 and 2 m, respectively. Four ventilation shafts are located near the entrance and exit of the station, whose cross-section is 5 m × 5 m and height is 30 m. Three types of PSDs were tested for comparison purposes. The fully sealed PSD is 2 m high, completely isolating the tunnel

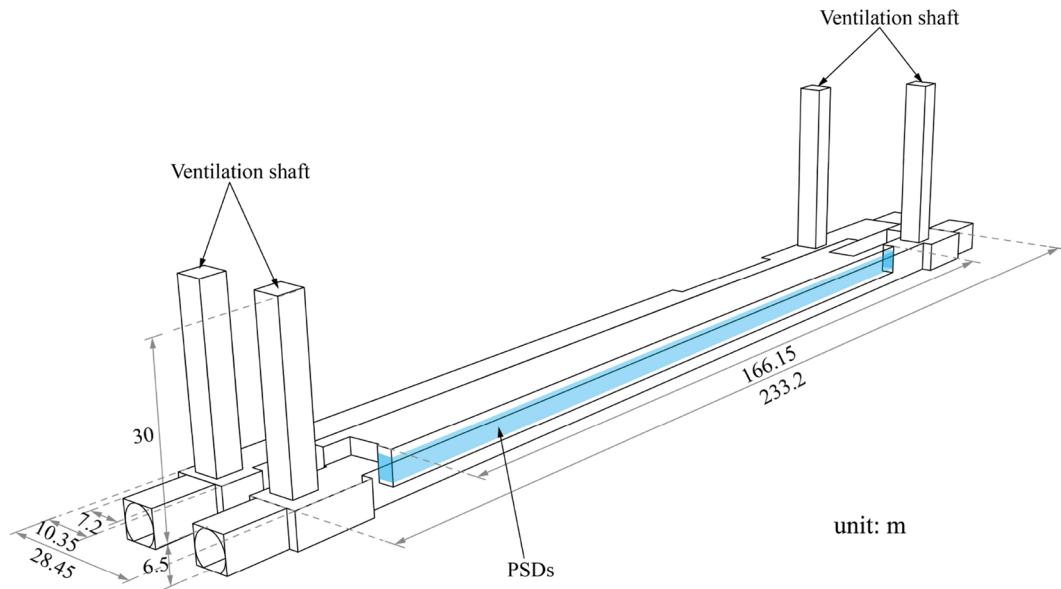


Fig. 1 3D sketch of a standard station with an island-type platform model

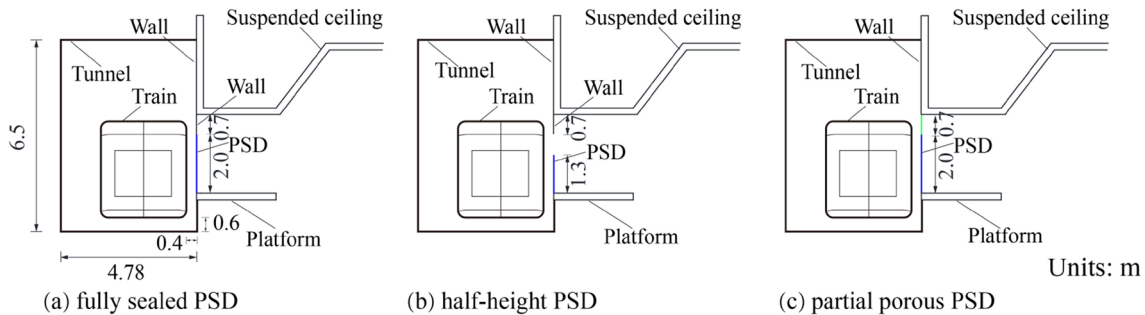


Fig. 2 Three types of PSDs calculated for the non-stop cases: **a** fully sealed, **b** half-height, and **c** partial porous

and platform when closed (Fig. 2a). The half-height PSD is 1.3 m high, resulting in a connection of the tunnel with the platform space, as shown in Fig. 2b. The height of the partial porous PSD is also 2 m. A 0.7 m gap between the PSD and ceiling was filled with plates with a porous ratio of 50% (Fig. 2c).

Figure 3a gives the locations of pressure taps on the PSDs. Particularly, taps 1 and 8 were arranged at the end-door of PSDs close to the entrance and exit of the station, respectively, while taps 2 to 7 were placed on the PSDs along the platform. All taps were located at the mid-height of the PSDs. The distance between two adjacent taps was about 23.8 m. The train used in the present simulation was a classical type A+ train consisting of eight coaches (Fig. 3b), which is extensively used in metro systems all around China. The length, height, and width of the train were about 185 m, 3.36 m, and 3 m, respectively. Figure 3c gives the cross-sectional dimensions of the tunnel, which was a circle with a diameter of 7.2 m, except for the flat track bed at the bottom. Thus, the blockage ratio caused by the train was $\beta = 26.7\%$. For the cases of fully sealed PSDs, the tunnel in the station was rectangular, with a height of 6.5 m and a width of 4.78 m. Thus, the corresponding β was about 32.4%, slightly higher than that of the circular tunnel. The train is 0.6 m above the ballast and 0.4 m away from the PSDs, as shown in Fig. 2a.

The total length of the computational domain was 7863 m, including the 233.2 m-long station; the 5129.8 m long tunnel 1, connecting with the entrance of the station (highlighted in red in Fig. 4); and the 2500 m-long tunnel 2, connecting with the exit of the station (highlighted in blue in Fig. 4). For the implementation of moving mesh, the train and tunnel were separated by a virtual interface, as shown in Fig. 3d, which is used to exchange data between the sliding components [24, 25]. The surface of the train and the interface were discretized into unstructured hexahedral grid, with a minimum size of 0.01 m and a growth ratio of 1.15 in the wall-normal direction. The computational domain was also discretized into unstructured hexahedral meshes (Fig. 4), with a grid number of about 23 million. The total number of meshes for a train was about 2 million. The tunnel mesh part was stretched along the x direction after generating a hexahedral mesh in the inlet or outlet surface; the grid layer distance along the x direction is about 0.5 m. The minimum grid size on the tunnel and station parts was 0.1 m.

The boundary conditions at the tunnel entrance and exit were set as pressure-out and non-reflecting, which can prevent the reflection of the pressure waves [26, 27]. The surfaces of the train, tunnel, and PSDs were set as no-slip walls. It is worth mentioning that all ventilation shafts were connected with a large space at their upper exit, as shown in Fig. 4, which can effectively reduce the

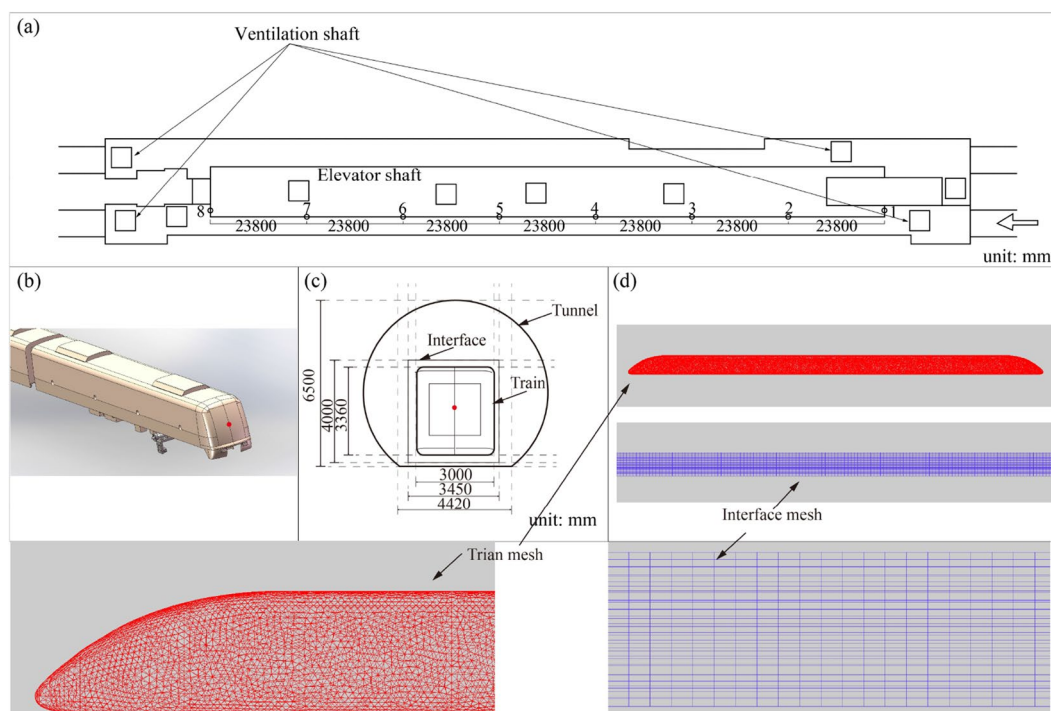


Fig. 3 a Station section and pressure taps on PSDs; b 3D sketch of the type A+ subway train model; c cross section dimension of the tunnel model; d the mesh of the train and interface

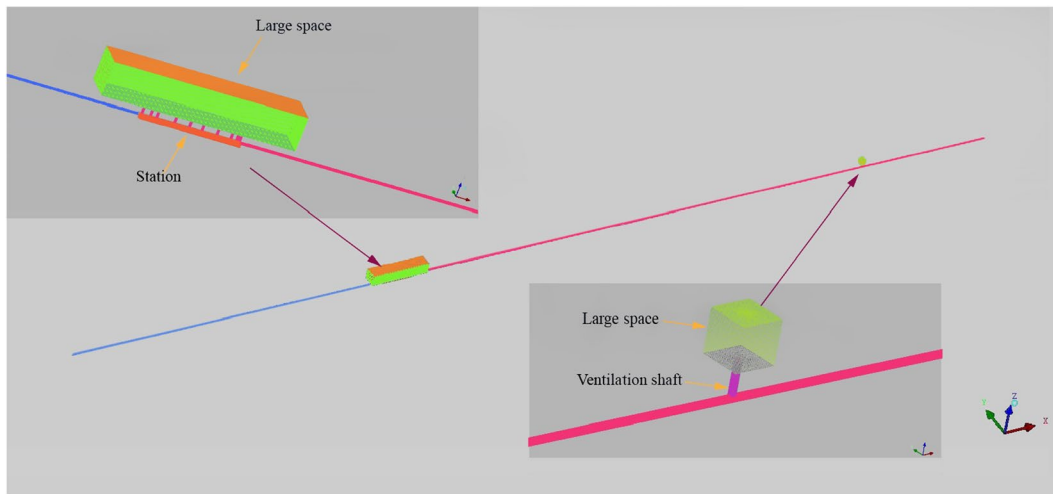


Fig. 4 Computational mesh

computation divergence caused by defining the boundary condition at the exit of the ventilation shafts [28]. The boundary condition of the sides and top surfaces of the large space was pressure-out, reflecting, while the bottom surface was defined as a solid wall.

2.2 Mathematical Model

The Reynolds number, based on the maximum train speed (140 km/h) and the width of the train (3 m), reaches 7.896×10^6 . The flow inside the tunnel is usually regarded as a three-dimensional unsteady compressible flow [13, 29]. Based on the Reynolds-averaged Navier–Stokes (RANS) equations, Liu et al. [30–31] Ogawa and Fujii [32], , Niu et al. [33], and Yuan et al. [13] have successfully captured the dynamic pressure generated by a train passing through a tunnel or station. The renormalization group (RNG) k - ϵ model has been widely adopted for analyzing the pressure variations inside tunnels or stations [13, 15, 33, 34]. Thus, we adopted the RNG k - ϵ model in the present simulation. The governing equations are as follows:

Mass equation:

$$\frac{\partial \rho}{\partial t} + \frac{\partial(\rho u_i)}{\partial x_i} = 0 \tag{1}$$

where u_i represents the velocity component in i direction, $i = 1, 2,$ and 3 . t is the time and ρ is the fluid density.

RANS equation:

$$\rho \left(\frac{\partial u_i}{\partial t} + u_k \frac{\partial u_i}{\partial x_k} \right) = -\frac{\partial p}{\partial x_i} + \frac{\partial}{\partial x_j} \left(\mu \frac{\partial u_i}{\partial x_j} \right) + \frac{\partial R_{ij}}{\partial x_j} \tag{2}$$

where p and μ represent the averaged pressure and air dynamic viscosity, and $R_{ij} = -\rho \overline{u'_i u'_j}$ is the Reynolds stress

tensor, which can be solved based on the Boussinesq equation:

$$R_{ij} = -\overline{\rho u'_i u'_j} = \mu_t \left(\frac{\partial u_i}{\partial x_j} + \frac{\partial u_j}{\partial x_i} \right) - \frac{2}{3}(\rho k)\delta_{ij} \tag{3}$$

where μ_t is the turbulent viscosity and $\mu_t = C_\mu \frac{k^2}{\epsilon}$, and $C_\mu = 0.0845$; δ_{ij} is the Kronecker delta function.

The equation for turbulence kinetic energy k :

$$\frac{\partial(\rho k)}{\partial t} + \frac{\partial(\rho k u_i)}{\partial x_i} = \frac{\partial}{\partial x_i} \left(a_k \mu_f \frac{\partial k}{\partial x_i} \right) + G_k + \rho \epsilon \tag{4}$$

And the equation for turbulence dissipation rate ϵ :

$$\frac{\partial(\rho \epsilon)}{\partial t} + \frac{\partial(\rho \epsilon u_i)}{\partial x_i} = \frac{\partial}{\partial x_j} \left(a_\epsilon \mu_f \frac{\partial \epsilon}{\partial x_j} \right) + \frac{C_{1\epsilon} \epsilon}{k} G_k - C_{2\epsilon} \rho \frac{\epsilon^2}{k} \tag{5}$$

where a_k and a_ϵ are the turbulent Prandtl constant, and $a_k = a_\epsilon = 1.39$; μ_f represents the dynamic viscosity, and $\mu_f = \mu + \mu_t$; G_k is the turbulent kinetic energy generated by the mean velocity gradients; $C_{1\epsilon}$ and $C_{2\epsilon}$ are model coefficients, and $C_{2\epsilon} = 1.68$.

$$C_{1\epsilon} = C_\epsilon - \frac{\eta \left(\frac{\eta}{\eta_0} \right)}{1 + \beta \eta^3} \tag{6}$$

where $C_\epsilon = 1.42$, $\eta_0 = 4.377$, and $\beta = 0.012$, $\eta = (2E_{ij} \cdot E_{ij})^{1/2} \frac{k}{\epsilon}$, E_{ij} is the time-averaged strain rate.

These governing equations are numerically solved by the finite volume method (FVM) using ANSYS Fluent commercial code. The PISO (Pressure-Implicit with Splitting of Operators) algorithm is used to deal with the coupling between pressure and velocity. The convection and diffusion

terms are discretized by adopting a second-order upwind scheme. An implicit scheme with second-order accuracy is used to solve the time term. The residual of each turbulent equation is set at 10^{-5} to guarantee convergence. All numerical calculations were conducted on the Tianhe II supercomputer at the National Supercomputing Center, Hunan. For each simulation, 200 CPUs were used. The time step in the present simulation was set as 0.001 s, and the total duration for one case was about 12 days (simulated physical time) and 150 s (simulation time used on the computing platform). As such, the maximum displacement of the moving mesh is about 0.0389 m at 140 km/h, which should be small enough compared to the grid distance along the tunnel (roughly about 0.5 m) to guarantee the accuracy of the simulation. In addition, we have validated our simulation results with the moving model test results of Zeng et al. [6], which agree with each other quite well. Therefore, for saving computing resources based on the full-scale simulation, the time step of 0.001 s was adopted in the present calculation.

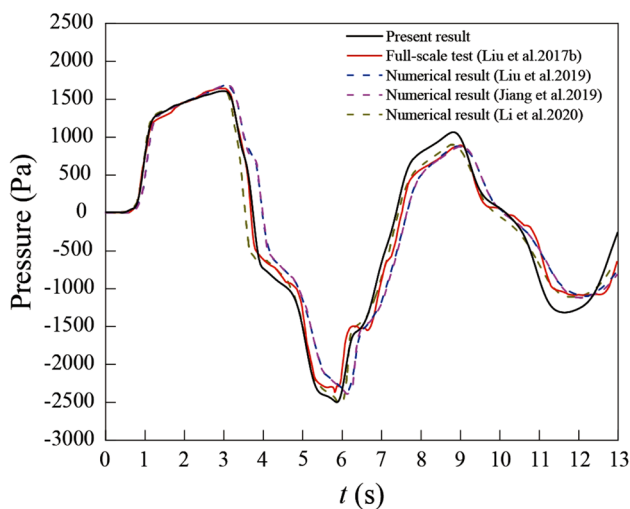
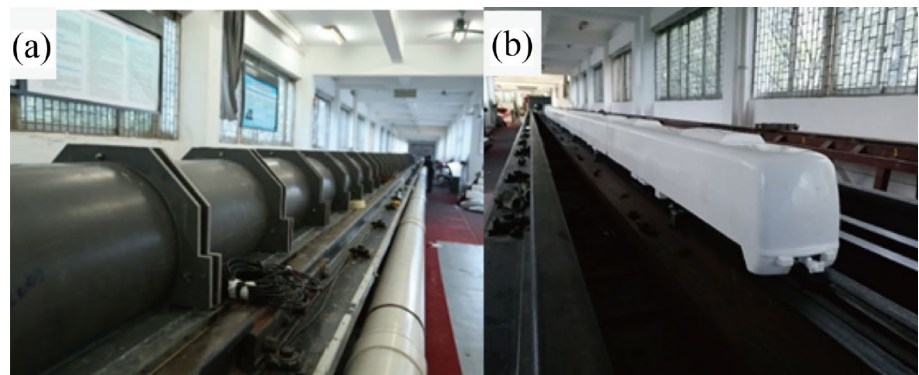


Fig. 5 Pressure variation at 300 m from the tunnel entrance of a 1005 m-long tunnel. Train type: CRH2C, train speed: 300 km/h, train-induced blockage ratio of the tunnel: 12.5%

Fig. 6 Photos of the moving model test: **a** tunnel model; **b** train model

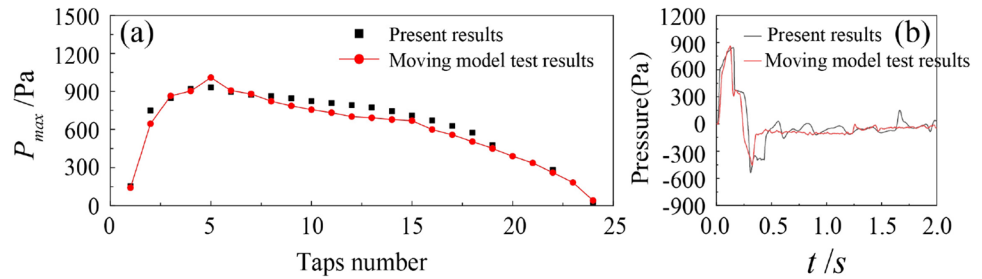


2.3 Validation

To confirm the applicability and accuracy of the present numerical method, we repeated the case reported by Liu et al. [30] for a CRH2C (China Railway High-speed 2C) high-speed train passing through a tunnel at a speed of 300 km/h. The tunnel length is 1005 m and the blockage ratio caused by the train is 12.5%. Other detailed information for this case can be found in Liu et al. [30]. Figure 5 compares the pressure variation at a point 300 m from the tunnel entrance with those reported by Liu et al. [11], Liu et al. [30], Jiang et al. [35], and Li et al. [36] based on their field test and numerical simulation. Generally, the present result agrees well with those reported in the literature. Compared with the full-scale field test, the maximum positive and negative pressure errors are 2.01% and 2.04%, respectively, and the peak-to-peak error is 0.42%.

The pressure variation inside a 51.6 m tunnel caused by a subway train was also simulated using the above-mentioned sliding mesh technique. The train speed is 120 km/h, and the blockage ratio of the tunnel is 26.7%. The maximum pressure P_{\max} along the tunnel is compared with the data given by Zeng et al. [6], which was obtained using the moving model test, as shown in Figs. 6 and 7. Readers may refer to Zeng et al. [6] for more details about this case and their test facilities. Note that the scale ratio (1:20) of the present simulation was identical to the moving model test [6]. As shown in Fig. 7, the distribution of P_{\max} along the tunnel is consistent with the experimental result. The extreme P_{\max} appears at 10.3 m from the tunnel entrance, which is 935 Pa in the present simulation and 1026 Pa in the moving model test. The deviation between them is 8.86%. The time history of the pressure at 6.2 m from the tunnel entrance is also compared in Fig. 7b. The present simulation successfully captured the primary positive and negative pressure waves. In addition, several small fluctuations of the pressure are observed in the simulation result, as shown in Fig. 7b, which are absent in the moving model test. This difference should be ascribed to the reflection of the pressure wave at the tunnel's entrance and exit. Apparently, the numerical

Fig. 7 Comparison of the extreme pressure along the tunnel of the present results with that of Zeng et al. [6]: **a** P_{max} and **b** time-history pressure at 6.2 m from the tunnel entrance



simulation slightly overestimated the reflection compared with the moving model test. Considering the general agreements in the comparison shown in Figs. 5 and 7, the numerical technique described in Sects. 2.1 and 2.2 is appropriate for the present study.

3 Results and Discussion

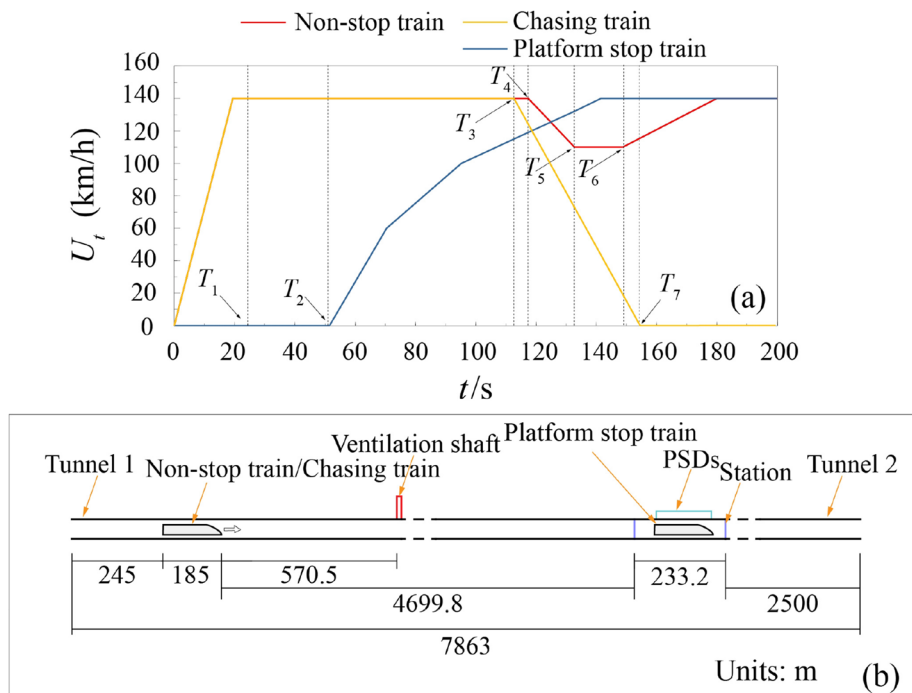
3.1 Non-stop Cases and Chasing Cases

Figure 8a presents a diagram of the train speed for the non-stop and chasing cases in real metro running scenarios. The relative positions of the train, tunnel, and station are presented in Fig. 8b. In the non-stop cases, at $t = 0$ s, the train inside the tunnel accelerates with constant acceleration $a = 2 \text{ m/s}^2$. The train is initially in the tunnel, 245 m away from its entrance, to avoid forming significant pressure waves as the train directly enters the tunnel. Once the speed reaches $U_t = 140 \text{ km/h}$, the train continues running at this constant

speed until it approaches 506 m from the station, as indicated by T_4 in Fig. 8a. The train gradually decelerates to $U_t = 110 \text{ km/h}$ when it arrives at the station entrance (as represented by T_5) and then passes the station at this constant speed. When the train passes the station at T_6 , it accelerates again to $U_t = 140 \text{ km/h}$. The different speed modes, including the speed-changing mode, were realized by defining the profile in Fluent. In that profile, we can define the time and corresponding speed for the train.

In the chasing case, the running scenario of the coming train is identical to the non-stop case until T_3 . It starts to decelerate constantly and stops at the platform at T_7 . Note that before T_3 , the stopped train inside the station has already begun to accelerate and leave the platform at T_2 . In other words, the stopped train will leave the station when the coming train is about 3 km away. It is worth mentioning that there is a ventilation shaft in tunnel 1, which is 570.5 m ahead of the initial position of the coming train (as shown in Fig. 8b). The coming train reaches the shaft at 24.4 s (T_1) after its speed reaches 140 km/h.

Fig. 8 **a** the departure schedule in real metro running scenarios and **b** the relative position of the train, tunnel, and station



To investigate the pressure variations on the train, we placed a pressure tap at the train head (as highlighted by the red point in Fig. 3b and c); the time-history pressure curve of the train head is depicted in Fig. 9. The pressure of the train head rapidly increases to 1615 Pa at time A ($t = 19.44$ s) during the first acceleration part. This is because the airflow in front of the train head is squeezed, as shown in Figs. 10a and 11a, similar to that was observed by Niu et al. [33] and Zhou et al. [3]. This part of the pressure is mainly decided by the slipstream [37–39], the length of which is about 200 m

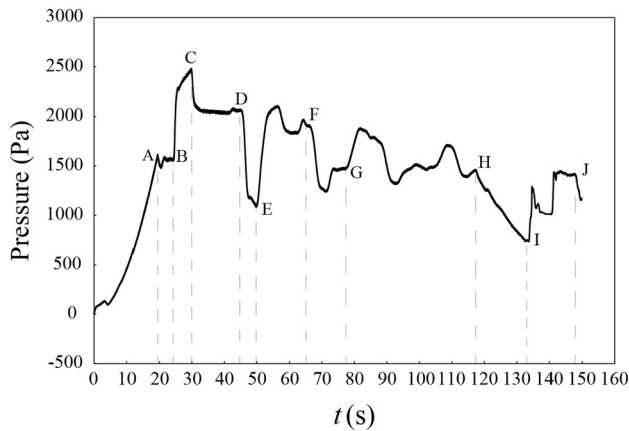


Fig. 9 The pressure variations on the train head for a non-stop train passes by the station

(from the location of the train head to the shaft of the tunnel). The pressure after the ventilation shaft is almost zero, as presented in Fig. 12a at $t = 20$ s. This observation indicates that the high-pressure region influenced by the train is limited, and the nearby ventilation shaft can significantly reduce the pressure associated with the slipstream.

The pressure of the train head remains relatively stable from time A to B. Afterward, the train head passes the shaft of the tunnel and generates a compression wave similar to that induced when a train enters a tunnel [6]. Therefore, the pressure rapidly increases, resulting in the maximum $P_{\max} = 2485$ Pa at time C (Fig. 9). Moreover, the flow field in front of the train is in a large positive pressure state and maintains a long transmit distance at $t = 27$ s, as shown in Figs. 10b and 11b. A similar observation was also reported by Kim and Kim [40], and Xiang et al. [41]. More specifically, the length of the high-pressure area originates from about 272 to 1090 m and then rapidly decreases to zero at around 1450 m, forming an approximately 1178 m pressure-affected region (Figs. 10b, 11b, and 12). Note that the origin and end of the coordinate in Fig. 12 were defined 140 m away from the tunnel shaft (at which the train speed reaches 140 km/h and runs at this constant speed) and the station's end, respectively (Fig. 12). In addition, this part of the pressure is the collective result of the slipstream and compression wave, which is obviously longer than that caused by the slipstream only. Since the P_{\max} of the train head is about 2485 Pa (Fig. 9), we can roughly estimate that the pressure

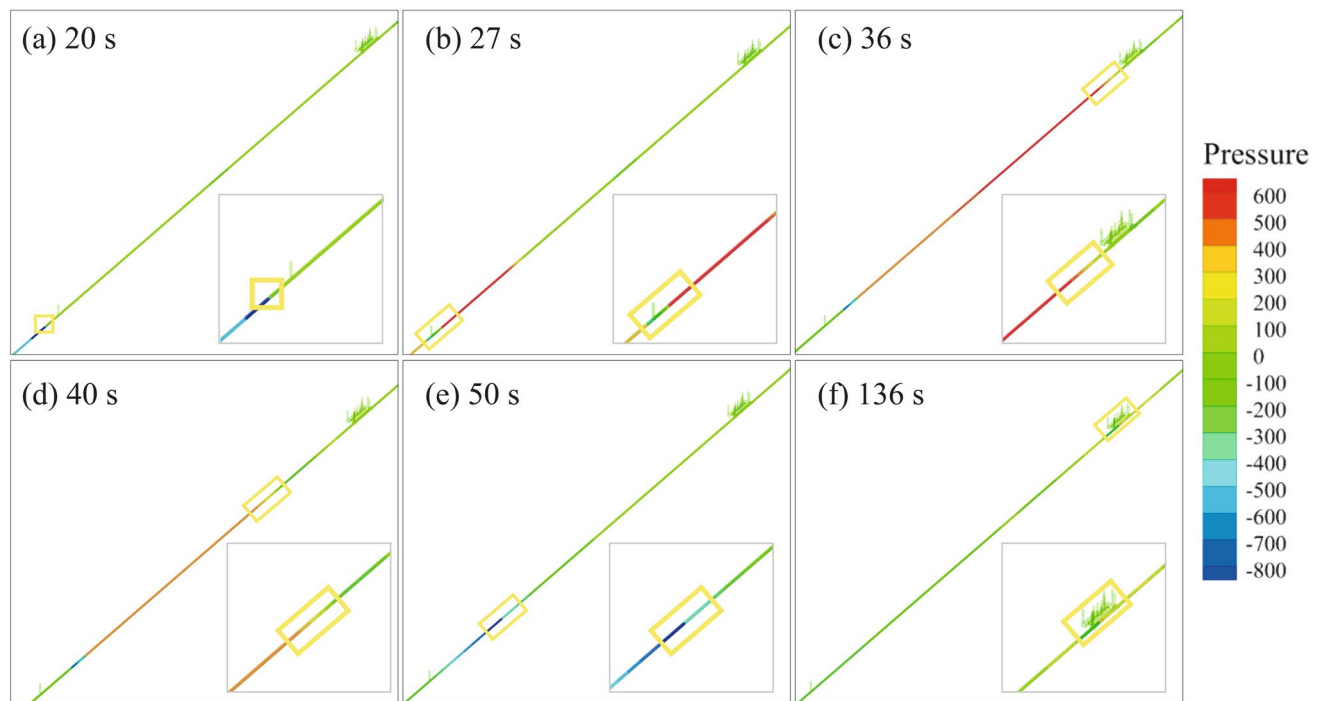


Fig. 10 Instantaneous pressure distribution at typical times for the non-stop train case

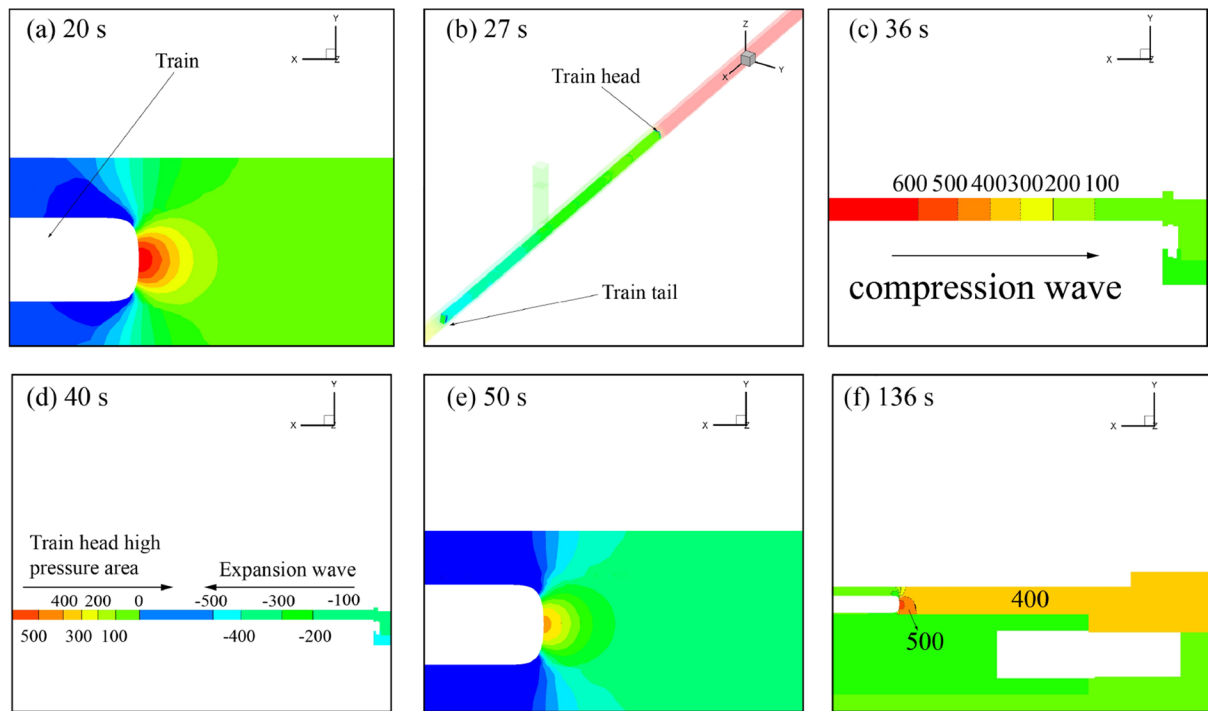


Fig. 11 Instantaneous pressure distribution at typical times for the non-stop train case with partial detail enlargement marked by the yellow squares in Fig. 9. The pressure label is identical to Fig. 9

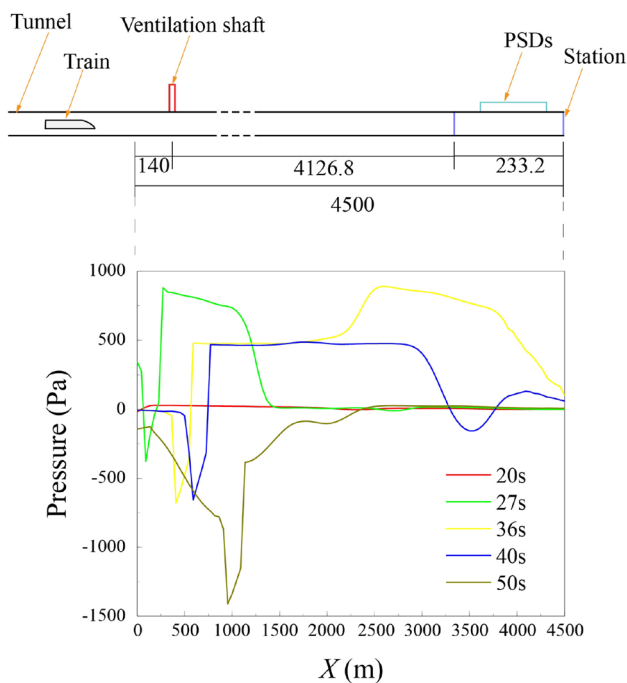


Fig. 12 Transient pressure distribution along the tunnel at typical times

caused by the compression wave is about 870 Pa, contributing about 35% of the P_{max} . This observation is consistent with that observed in Fig. 12, where the extreme pressure inside the tunnel associated with the compression wave is about 880 Pa at $t = 27$ s.

As mentioned, once the train tail passes the ventilation shaft, an expansion wave will be induced and transmitted to the station through the tunnel. Time C in Fig. 9 corresponds to the instant when the expansion wave propagates to the train head, as evidenced by a sharp decrease in pressure. Then, the pressure remains stable at around 2000 Pa for 30–45 s. The generated expansion wave continues to propagate along the tunnel and reduces the pressure inside the tunnel (see Figs. 9, 10c, and 12). However, the pressure of the train head from C to D is significantly higher than the pressure at times A to B. This is possible because when its head approaches the shaft and generates a compression wave, it increases the pressure on the train head, as indicated in Fig. 12. On the other hand, when its tail passes the shaft, the train may restrain the propagation of the expansion wave along its running direction due to the blockage effect.

The generated compression wave transmits to the station at the speed of sound, thus, it arrives at around 36 s. Figures 10c and 11c show the corresponding pressure distribution. It is seen that the pressure inside the station is mainly affected by the compression wave because, at that time, the train was about 3670 m away from the station,

and the affected regions of the slipstream were limited. This observation further confirms the finding reported by Zeng et al. [6] that the compression wave dominates the first peak associated with a non-stop train passing by a station, which is also suitable for real metro running scenarios. In addition, the pressure inside the station affected by the compression wave is around 200 Pa, as exhibited in Figs. 10c and 11c, which will be discussed in the following part. If we focus on the transient pressure distribution along the tunnel at $t = 36$ s, the pressure is about 790 Pa at the station entrance and sharply decreases along the station (Fig. 12). This attenuation of the compression wave is caused by two main reasons: the sudden increase in the tunnel cross-section area between the tunnel and station, and the operation of the station ventilation shafts.

Due to the reflection of the shafts and the large space of the station, the generated compression wave transforms into an expansion wave and then propagates back to the non-stop train [6]. At $t = 40$ s, the interaction of the high-pressure area (consisting of slipstream and pressure wave) and the expansion wave is quite apparent, as shown in Figs. 10d, 11d, and 12. This backward transmit process of the expansion wave can be represented by the pressure distribution changes from $t = 40$ to 50 s (Fig. 12), corresponding to the sharp drop of the pressure from time D to E in Fig. 9. The extreme pressure at time E is about 1085 Pa, which corresponds to the second compression wave (induced by the expansion wave encountering the shaft of the tunnel) reaching the position of the train head (Figs. 10e, 11e, and 12), and the pressure of the train head starts to rise again (Fig. 9). Interestingly, the pressure around time F is slightly smaller than that at time D. This is because the pressure waves attenuate obviously during their propagation and reflections [32, 42].

At around 68 s, the second expansion wave transmits to the train head, and the pressure drops again (Fig. 9). Time G in Fig. 9, corresponding to the third compression wave reaches the train head position and the pressure rises again. Afterward, the train decelerates to $U_t = 110$ km/h, resulting in the almost linear pressure decrease from time H to I (Fig. 9). The times I and J are related to the train head entering the station and the train tail leaving the station, respectively. The flow near the train head comes with a significant positive pressure as the train passes by the station, resulting in a sharp pressure increase on the PSDs [3]. Moreover, Figs. 10f and 11f present the pressure distribution at $t = 136$ s when the train passes the station. Clearly, a high-pressure region appears in front of the train head, indicating that the extremum pressure on PSDs ranges from 500 to 600 Pa for a train passing through the station.

Previous studies suggest that the extremum pressure on the PSD is highest near the station entrance, and decreases slightly along the PSD [40, 41, 43]. Therefore, only the time history of pressure at tap 1 is shown for straightforward

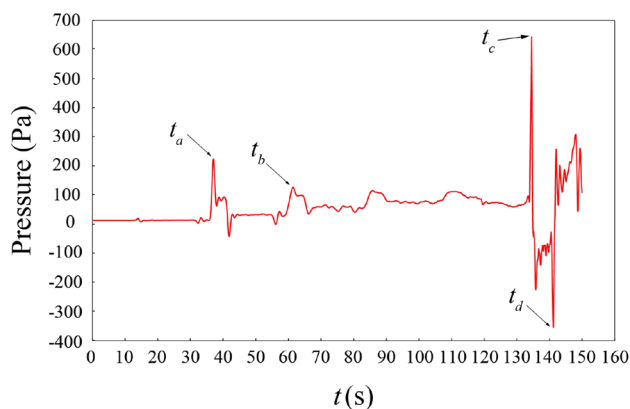


Fig. 13 Transient pressure on fully sealed PSD for non-stop cases: tap 1 at the end PSD

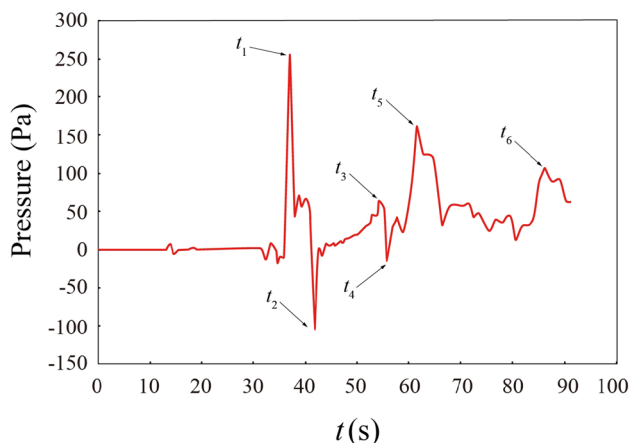


Fig. 14 Transient pressure on fully sealed PSD for chasing cases: tap 1 at the end PSD

data interpretation. Figure 13 shows the time-history pressure obtained at tap 1 on the fully sealed PSD for the non-stop case, where tap 1 was installed on the end of the PSD (see Fig. 3a for the locations of these taps). The pressure caused by the first compression wave on tap 1 is 212 Pa, as marked by time t_a in Fig. 13. On the contrary, the pressure is 252 Pa at tap 1 for the chasing case (Fig. 14). Compared with the non-stop case, the first positive peak pressure on PSD increases by about 18.87% for the chasing case. This phenomenon is obviously related to the blockage effects induced by the stopped train [6]. In addition, the time of the pressure acting on the PSDs for the non-stop and chasing cases is around 5.7 s (from 35.8 to 41.5 s). This lateral pressure on the PSDs may lead to extra friction resistance during their opening or closing process, which might be one reason for the PSD accident in the subway system. With the compression wave switches to the expansion wave, the pressure on the PSDs for the non-stop case and the chasing

case is immediately reduced, and relatively lower pressure is maintained for a while (Figs. 13 and 14).

Due to the attenuation of pressure waves during their propagation and reflections, the pressure on PSDs affected by the second compression wave is significantly weaker than the first one (as indicated by t_a and t_b in Fig. 13 and t_1 and t_2 in Fig. 14); this observation is similar to that observed in Fig. 9. Moreover, the positive and negative peak pressure at tap 1 is generated by the head and tail of the non-stop train (Fig. 13). This positive peak pressure on tap 1 is about 625 Pa. In contrast, the negative peak pressure on tap 1 is about -344 Pa. Note that the positive pressure on PSDs immediately turns negative after the train head passes by. The negative pressure immediately changes to positive after the train tail passes by. This phenomenon is consistent with that reported by Zhou et al. [22] and Wang [2].

For the chasing case, the pressure fluctuations are more evident than in the non-stop case, possibly because of the blockage effects caused by the platform-stopped train. Subsequently, the platform stop train slowly accelerates until it leaves the station (see Fig. 8a); thus, the pressure on tap 1 gradually rises, corresponding to the times from t_2 to t_3 in Fig. 14. The pressure at t_5 and t_6 are caused by the second and third compression waves, respectively.

3.2 Non-stop Cases with Different Forms of PSDs

Since the pressure on PSDs is mainly determined by pressure waves produced when the train head and tail pass by [3, 6, 13, 22], we simulated a non-stop train passing by a standard station without the tunnel ventilation shaft to distinguish the effect of pressure waves caused by the tunnel ventilation shaft. Meanwhile, to reduce the grid number and improve computational efficiency, the length of tunnels 1 and 2 has been reduced to 1000 m and 500 m, respectively. The non-stop train starts with a constant acceleration $a = 2 \text{ m/s}^2$ and then runs at a continuous speed $U_t = 110 \text{ km/h}$. The transient pressure on different forms of PSDs, i.e., fully sealed, half-height, and partial porous PSDs, has been compared. The train passes a fully sealed PSD with the station ventilation shafts closed was also calculated for comparison. The arrangement of the pressure taps on PSDs is shown in Fig. 3a.

The horizontal axis in Fig. 15 is the normalized length of the platform L^*_{PSD} . P_{max} and P_{min} on the fully sealed PSD with the shafts closed are about 773 Pa and -1011 Pa, respectively (Fig. 15). Once the shafts are open, the pressure on the fully sealed PSD obviously decreases. P_{max} and P_{min} on the PSD are about 550 Pa and -460 Pa, decreased by about 28.8% and 54.5%, respectively, similar to that observed by Yuan and You [43], Huang et al. [24], Zhang et al. [15], Meng et al. [19], and Zeng et al. [6].

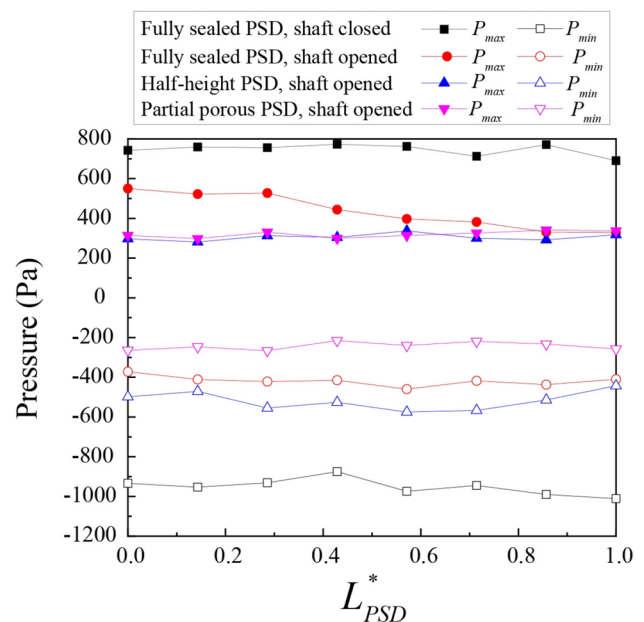


Fig. 15 Extreme pressure along the PSDs for different cases

For the half-height and partial porous PSDs, P_{max} decreases significantly compared to the fully sealed PSD, as exhibited in Fig. 15. For example, P_{max} on the half-height and partial porous PSDs are approximately 337 Pa and 341 Pa, respectively, reduced by 38.7% and 38.2% if compared to the fully sealed PSD. This is attributed to the fact that for both the half-height and partial porous PSDs, the track area and platform area are connected, which can help suppress the strength of the pressure waves and pressure generated by the passing of the train. As for P_{min} , the partial porous PSD also works well to suppress the negative pressure mainly caused by the train tail, with a minimum pressure of $P_{min} = -266 \text{ Pa}$ and a reduction of 42.2% compared with the fully sealed PSD (Fig. 15). In addition, the reduction effect of P_{max} gradually decreases along the PSD for both half-height and partial porous PSDs, as shown in Fig. 15. However, adopting the half-height PSD may slightly increase the negative pressure load on the PSD more than the fully sealed PSD. The possible reasons are that, firstly, a cavity structure is formed using the half-height PSD, and the corresponding resonance may increase negative pressure. Secondly, new pressure waves may be generated due to the opening circumstance and influence the pressure on the PSD. Thirdly, this negative pressure on PSD may also be related to the wind environment inside the station.

For the non-stop train passing the fully sealed PSD, the maximum pressure P_{max} on PSDs is highest at the station entrance (tap 1) and decreases gradually along the PSD (Fig. 15), which is consistent with that observed by Yuan et al. [13], Zeng et al. [6], and Zhou et al. [3].

However, P_{\max} on the half-height and partial porous PSDs remains almost constant along the PSDs (Fig. 15). This indicates that adopting half-height and partial porous PSDs may benefit the PSD's structure design because we can choose the same relatively lower intensity standard with certain economic benefits. Therefore, if the pressure load on a fully sealed PSD is too high for structure design, half-height and partial porous PSDs are alternative choices.

Figure 16 shows the pressure distribution inside the station with different types of PSDs for the non-stop case. For the case with the station ventilation shafts closed, a high-pressure region appears in the rectangular tunnel when the train enters the station with fully sealed PSDs, which is apparently associated with the sudden contraction of the tunnel. This high pressure is uniformly distributed across the tunnel and decreases gradually along the tunnel axis with increasing distance from the train head, as shown in Fig. 16a. Once the station ventilation shafts are open, the high pressure inside the tunnel caused by the coming train is reduced to approximately one-fourth of its corresponding value in Fig. 16a with the shafts closed.

If half-height or partial porous PSDs are adopted, the platform area is connected with the tunnel, which causes a further reduction of the pressure inside the tunnel, as shown in Fig. 16c and d. However, the pressure variation and associated train-induced wind in the platform

area may cause additional serviceability problems for passengers.

4 Conclusions

The present study focused on investigating the aerodynamic loads on PSDs of a standard island-type platform using the moving mesh technique in conjunction with real scenarios and full-scale simulation. One of the key aspects examined was the effect of the ventilation shaft and different types of PSDs on the train-induced pressure. The main aim of the research was to provide guidance on optimizing the associated pressure/operation problem on the PSD. The conclusions are as follows:

- (1) As the train travels through the tunnel's ventilation shaft, it generates a compression wave that propagates along the tunnel towards the station, resulting in a notable pressure increase on the PSDs, even when the oncoming train is situated far from the platform. The maximum pressure on the PSDs is approximately 212 and 252 Pa for non-stop and chasing cases, respectively. This increase in lateral pressure on PSDs can lead to additional friction force during their opening or closing process, thereby possibly causing PSD failure during rush hours.

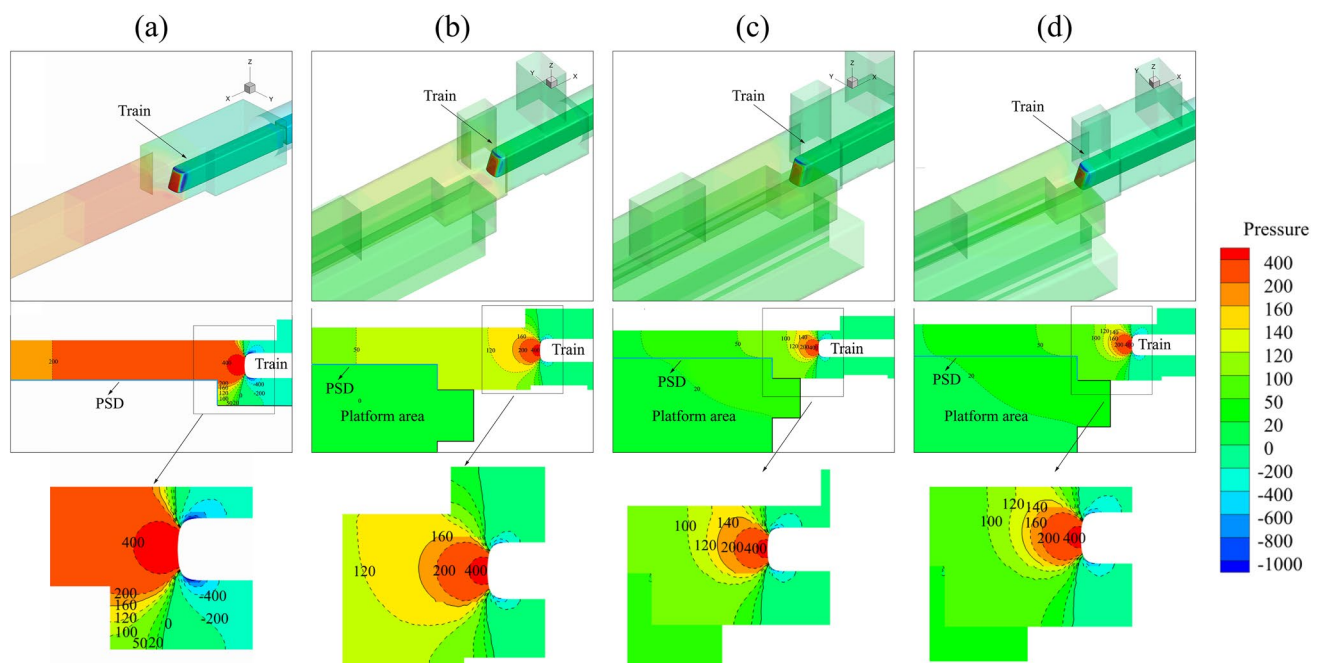


Fig. 16 Pressure distribution inside the station for the non-stop train case: **a** fully sealed PSDs with the station ventilation shafts closed; **b**, **c**, and **d** fully sealed, half-height, and partial porous PSDs with the station ventilation shafts opened, respectively

- (2) In the non-stop cases, we observed two positive and one negative pressure extremum during the entire process, where the compression wave mainly determines the first positive extreme pressure. On the other hand, the second positive and negative extreme pressure is caused by the passing train, with the train head and tail passing by, respectively. The peak pressure is highest at the entrance of the station (around 500–600 Pa when the train speed is 110 km/h) and subsequently decreases slightly along the platform. Interestingly, the P_{\max} for the half-height and partial porous PSDs remains almost constant along the PSDs, which could potentially benefit the design and economic savings.
- (3) Once the partial porous or half-height PSDs are used, the pressure on the PSDs related to the passing of the train head can be markedly reduced, especially at the station entrance. Moreover, the maximum pressure on the fully sealed PSD diminishes by 38.7% if half-height PSD is adopted and by 38.2% if partial porous PSD is adopted. These findings underscore the potential advantages of using partial porous or half-height PSDs in metro stations to address the pressure/operation problem on PSDs and increase the overall safety and reliability of these important components.

Our study provides valuable insights into the impact of different factors on train-induced pressure on PSDs, and could be of great assistance in optimizing related pressure/operation problems on these critical components of metro platforms.

Funding The authors wish to acknowledge the support given to them by the National Natural Science Foundation of China (Project No.: 52078505)

Declarations

Conflict of interest The authors declare that they have no conflict of interest.

Open Access This article is licensed under a Creative Commons Attribution 4.0 International License, which permits use, sharing, adaptation, distribution and reproduction in any medium or format, as long as you give appropriate credit to the original author(s) and the source, provide a link to the Creative Commons licence, and indicate if changes were made. The images or other third party material in this article are included in the article's Creative Commons licence, unless indicated otherwise in a credit line to the material. If material is not included in the article's Creative Commons licence and your intended use is not permitted by statutory regulation or exceeds the permitted use, you will need to obtain permission directly from the copyright holder. To view a copy of this licence, visit <http://creativecommons.org/licenses/by/4.0/>.

References

1. Qu L, Chow WK (2012) Platform screen doors on emergency evacuation in underground railway stations. *Tunn Undergr Spa Technol* 30:1–9
2. Wang XY (2017) Numerical analysis on aerodynamic behavior of high-speed trains in the tunnel and open air based on the virtual reality technique. *J Vibroeng* 20(2):1144–1160
3. Zhou YL, Wang HL, Bi YL, Wang J (2021) Experimental and numerical study of aerodynamic pressures on platform screen doors at the overtaking station of a high-speed subway. *Build Environ* 191:107582
4. Chen HH (2004) Mechanism design and mechanics model of the station screen doors for subways. *J South China Univ Tech* 32(2):74–77 ((in Chinese))
5. Han EW (2018) Switch fault of platform screen door caused by train piston wind pressure in Xi'an metro and improvements. *Urban Mass Transit* 191:148–151 ((in Chinese))
6. Zeng LW, Wang HF, Li LQ, Guo W, Yi FM (2021) Experimental study of train-induced pressure acting on the platform screen doors in subway station. *Tunn Undergr Spa Technol* 117:104150
7. Chun LJ, Chiang YC, Ting CC, Ma RH, Chen SL (2004) Pressure analysis of platform screen door subjected to a moving train in mass rapid transport underground station. *J Mech* 20(2):159–166
8. Du JM, Fang Q, Wang G, Zhang DL, Chen TL (2021) Fatigue damage and residual life of secondary lining of high-speed railway tunnel under aerodynamic pressure wave. *Tunn Undergr Space Technol* 111:103851
9. Kim JY, Kim KY (2007) Experimental and numerical analyses of train-induced unsteady tunnel flow in subway. *Tunn Undergr Spa Technol* 22(2):166–172
10. Liu TH, Chen ZW, Chen XD, Xie TZ, Zhang J (2017) Transient loads and their influence on the dynamic responses of trains in a tunnel. *Tunn Undergr Spa Technol* 66:121–133
11. Liu TH, Chen XD, Li WH, Xie TZ, Chen ZW (2017) Field study on the interior pressure variations in high-speed trains passing through tunnels of different lengths. *J Wind Eng Ind Aerod* 169:54–66
12. Baron A, Molteni P, Vigevano L (2006) High-speed trains: prediction of micro-pressure wave radiation from tunnel portals. *J Sound Vib* 296(1–2):59–72
13. Yuan H, Zhou D, Shuang M (2019) Study of the unsteady aerodynamic performance of an inter-city train passing through a station in a tunnel. *Tunn Undergr Spa Technol* 86:1–9
14. Raghunathan RS, Kim HD, Setoguchi T (2002) Aerodynamics of high-speed railway train. *Prog Aerosp Sci* 38(6):469–514
15. Zhang G, Kim TH, Kim DH, Kim HD (2018) Prediction of micro-pressure waves generated at the exit of a model train tunnel. *J Wind Eng Ind Aerod* 183:127–139
16. Matsuo K, Aoki T (1992) Wave problems in high-speed railway tunnels *Shock Waves*. Springer, Berlin
17. Ricco P, Baron A, Molteni P (2007) Nature of pressure waves induced by a high-speed train travelling through a tunnel. *J Wind Eng Ind Aerod* 95:781–808
18. Mei YG (2013) A generalized numerical simulation method for pressure waves generated by high-speed trains passing through tunnels. *Adv Struct Eng* 16(8):1427–1436
19. Meng S, Zhou D, Wang Z (2019) Moving model analysis on the transient pressure and slipstream caused by a metro train passing through a tunnel. *PLoS ONE* 14(9):e0222151
20. Luo JJ (2016) Study on the aerodynamic characteristics of tunnel and metro station with PSD during high-speed train passing tunnel. *Int J Signal Process* 9(6):379–392

21. Kim JY (2010) Field experiment of train-induced wind pressure on station screen door at subway station. *Int J Air-Cond Refrigeration* 18(04):309–316
22. Zhou D, Tian HQ, Zhang J, Yang MZ (2014) Pressure transients induced by a high-speed train passing through a station. *J Wind Eng Ind Aerod* 135:1–9
23. Liang XF, Chen G, Li XB, Zhou D (2020) Numerical simulation of pressure transients caused by high-speed train passage through a railway station. *Build Environ* 184:107228
24. Huang YD, Gao W, Kim CN (2010) A numerical study of the train-induced unsteady airflow in a subway tunnel with natural ventilation ducts using the dynamic layering method. *J Hydrodyn Ser B* 22:164–172
25. Shin CH, Park WG (2003) Numerical study of flow characteristics of the high speed train entering into a tunnel. *Mech Res Commun* 30:287–296
26. Choi JK, Kim KH (2014) Effects of nose shape and tunnel cross-sectional area on aerodynamic drag of train traveling in tunnels. *Tunn Undergr Spa Technol* 41:62–73
27. Kim TK, Kim KH, Kwon HB (2011) Aerodynamic characteristics of a tube train. *J Wind Eng Ind Aerod* 99:1187–1196
28. Juraeva M, Ryu KJ, Jeong SH, Song DJ (2013) A computational analysis of the airflow in a twin-track subway tunnel with a sliding-curtain to improve ventilation performance. *J Mech Sci Technol* 27(8):2359–2365
29. Yang WC, Peng LM, Wang LC (2009) Computation simulation on aerodynamic characteristic of PSD in subway station. In: *International conference on computer engineering & technique*. IEEE Computer Society
30. Liu TH, Jiang ZH, Li WH, Guo ZJ, Chen XD, Chen ZW, Krajinovic S (2019) Differences in aerodynamic effects when trains with different marshalling forms and lengths enter a tunnel. *Tunn Undergr Spa Technol* 84:70–81
31. Liu TH, Tian HQ, Liang XF (2010) Design and optimization of tunnel hoods. *Tunn Undergr Spa Technol* 25(3):212–219
32. Ogawa T, Fujii K (1997) Numerical investigation of three-dimensional compressible flows induced by a train moving into a tunnel. *Comput Fluids* 1:565–585
33. Niu JQ, Zhou D, Liang XY, Liu TH, Liu S (2017) Numerical study on the aerodynamic pressure of a metro train running between two adjacent platforms. *Tunn Undergr Spa Technol* 65:187–199
34. Chen Z, Liu T, Zhou X, Niu J (2017) Impact of ambient wind on aerodynamic performance when two trains intersect inside a tunnel. *J Wind Eng Ind Aerod* 169:139–155
35. Jiang ZH, Liu TH, Chen XD, Li WH, Guo ZJ, Niu JQ (2019) Numerical prediction of the slipstream caused by the trains with different marshalling forms entering a tunnel. *J Wind Eng Ind Aerod* 189:276–288
36. Li WH, Liu TH, Chen ZW, Guo ZJ, Huo XS (2020) Comparative study on the unsteady slipstream induced by a single train and two trains passing each other in a tunnel. *J Wind Eng Ind Aerod* 198:104095
37. Cross D, Hughes B, Ingham D, Ingham D, Ma L (2015) A validated numerical investigation of the effects of high blockage ratio and train and tunnel length upon underground railway aerodynamics. *J Wind Eng Ind Aerod* 146:195–206
38. Gilbert T, Baker CJ, Quinn A (2013) Gusts caused by high-speed trains in confined spaces and tunnels. *J Wind Eng Ind Aerod* 121:39–48
39. Wang F, Liu F, Han JQ, Jin HP, Weng MC, Zeng Z (2020) Study on the train-induced unsteady airflow in a metro tunnel with multi-trains. *Tunn Undergr Spa Technol* 106:103565
40. Kim JY, Kim KY (2009) Effects of vent shaft location on the ventilation performance in a subway tunnel. *J Wind Eng Ind Aerod* 97:174–179
41. Xiang XT, Xue LP, Wang BL, Zou W (2018) Mechanism and capability of ventilation openings for alleviating micro-pressure waves emitted from high-speed railway tunnels. *Build Environ* 132:245–254
42. Huang S, Che ZX, Li ZW, Jiang YN, Wang ZG (2020) Influence of tunnel cross-sectional shape on surface pressure change induced by passing metro trains. *Tunn Undergr Space Technol* 106:103611
43. Yuan FD, You SJ (2007) CFD simulation and optimization of the ventilation for subway side-station. *Tunn Undergr Spa Technol* 22:474–482